Geophysical Research Letters

Supporting Information for

Rupture Process of the 2020 Caribbean Earthquake along the Oriente Transform Fault, Involving Supershear Rupture and Geometric Complexity of Fault

Tira Tadapansawut[1], Ryo Okuwaki[2,3], Yuji Yagi[2], and Shinji Yamashita[1]

[1]Graduate School of Life and Environmental Sciences, University of Tsukuba, Tsukuba, Ibaraki 305-8572, Japan.
[2]Mountain Science Center, Faculty of Life and Environmental Sciences, University of Tsukuba, Tsukuba, Ibaraki 305-8572, Japan.
[3]COMET, School of Earth and Environmental, University of Leeds LS2 9JT, UK.

Corresponding author: Ryo Okuwaki (rokuwaki@geol.tsukuba.ac.jp)
Second corresponding author: Yuji Yagi (yagi-y@geol.tsukuba.ac.jp)

Contents of this file

Introduction

Figure S1 shows the waveform fitting for the optimal finite-fault. The uncertainty analyses of the finite-fault inversion are summarized in Text S1, Figures S2 to S9, and Tables S1 to S2. Figure S10 visualizes the relative weights for the basis double-couple components adopted our new finite-fault inversion. Figure S11 shows comparison between the conventional and new results adopting the relative weights for the basis double-couple components.

Text S1. Uncertainty and sensitivity analyses of the finite-fault inversion

We tested assumption of maximum rupture velocity at 3, 4, 5, and 6 km/s (Fig. S2). The initial and main rupture episodes were robustly resolved for all the assumptions of maximum rupture velocity. The assumption of maximum rupture velocity did not affect the temporal location of the main rupture episode at ~20–30 s. For the slower rupture velocity (≤ 3 km/s), the spatial location of the main rupture was arbitrary confined by the assumption of maximum rupture velocity, but it stayed stable at -100 km to -50 km for the faster rupture velocity ≥ 4 km/s. Later stages of rupture (e.g., > 50 s) shows less stable than the initial and main rupture stages against the assumption of maximum rupture velocity. The slight difference of the model-fault geometry did not affect the solutions. We applied the alternative model-faults: strike/dip at 77°/87° and 257°/87° to test the sensitivity of the different dip angle assumption of the model fault planes (Fig. S3). The resultant of total focal mechanism, moment-rate function, large potency density zone and the strike orientation change were consistent to our assigned model-plane in this study (strike/dip = 77°/90°, Fig 2). We further tested the assumption of model-fault geometry by adopting the horizontal model fault dipping at 0° placed at 15-km depth, in order to evaluate the spatial extents of rupture. As shown in Figs. S4 and S5, the spatiotemporal location of the initial and main rupture episodes share the similar feature between the two; the one with 0°-dipping and the other with the vertical dipping. The strike orientation at -320 to -220 km westward of the epicenter is also consistent between the two. The consistency against the model faults adopting the different dip angles can be explained by the very narrow, confined width of the rupture area for the 2020 Caribbean earthquake, which shows the less variable rupture manner along the dip extent of the fault. Moreover, we have extended the length along the strike of the model fault plane covering the mid-Cayman rise axis to evaluate the rupture termination (Figs. S6 and S7). Even if we extended the western side of model-fault length, we did not resolve the significant potency density across the mid-Cayman rise axis after 50 s.

We tested the assumption of maximum duration of potency-rate density function at each subfault, by reducing from 61 s to 41 s (Fig. S8). We found the initial and main rupture episodes were robustly resolved in both space and time and not contaminated by the assumption of rupture duration.

The different near-filed structural velocity models of CRUST1.0 and CRUST2.0 (Tables S1 and S2) were also tested to evaluate the sensitivity (Fig. S9). Although we recognize the slight difference between them, but the assumption of near-field velocity structure did not significantly affect the solution.

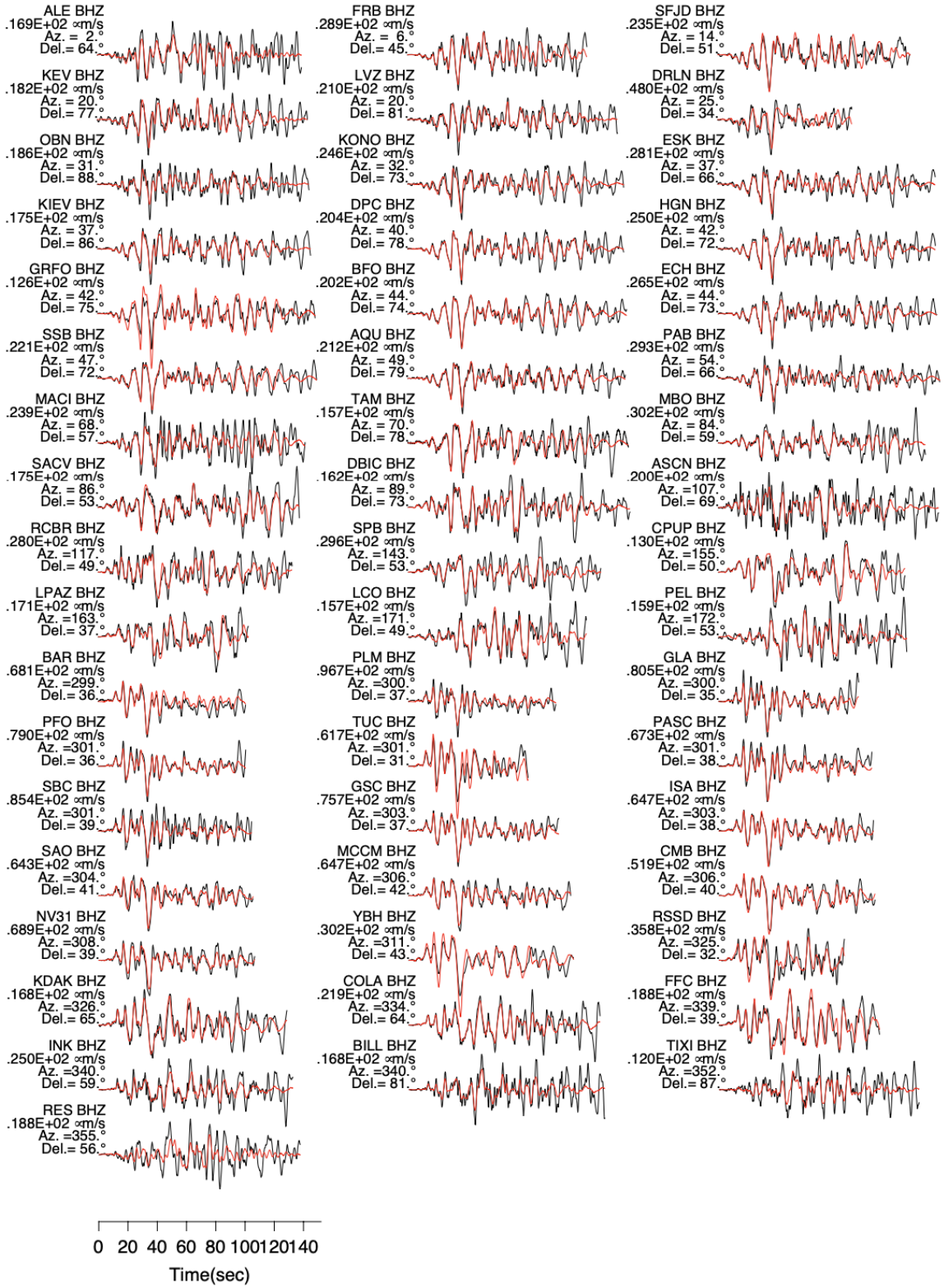

Figure S1. Waveform fitting at all stations between observed (black) and synthetic waveforms (red). Station code, azimuth, and epicentral distance are shown on top-left of the waveform.

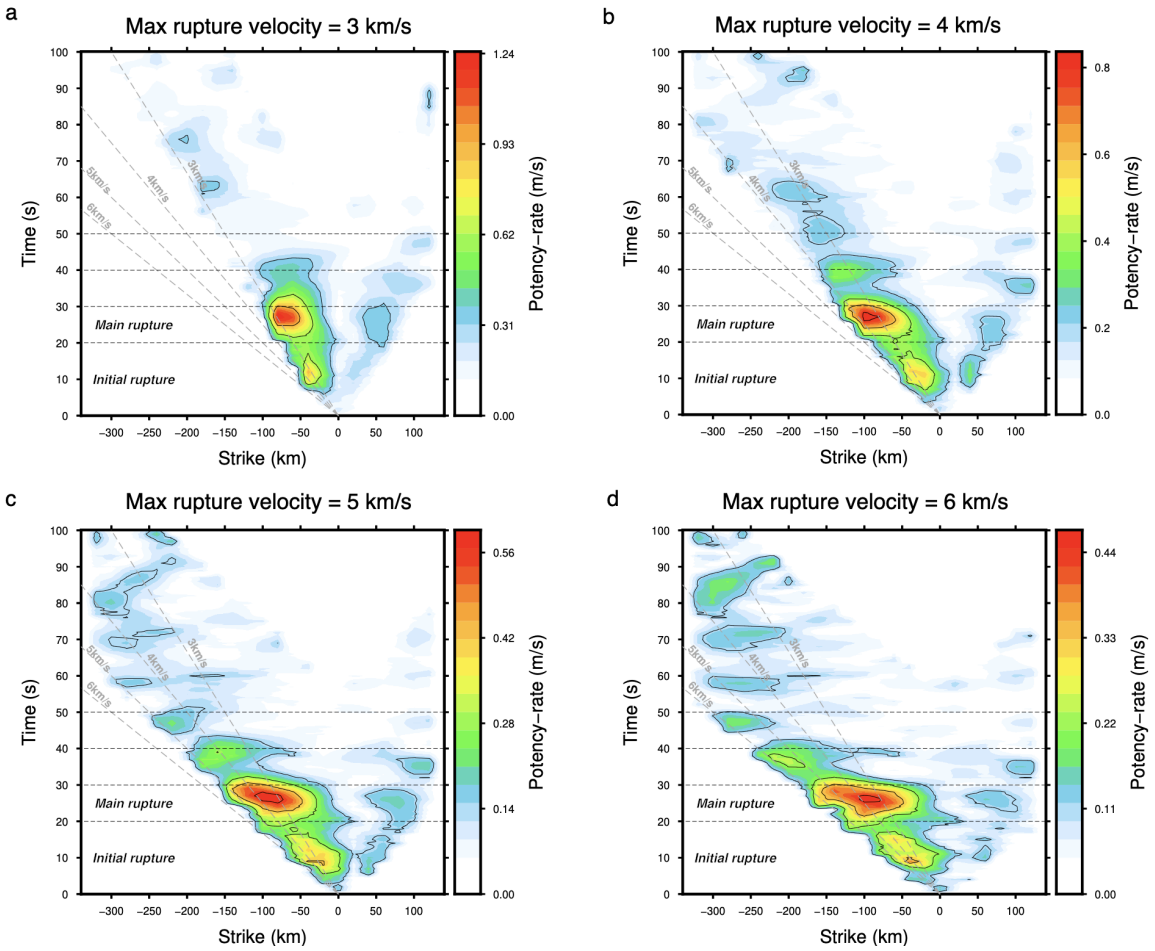

Figure S2. The comparison of spatiotemporal distribution of potency-rate density along the strike. Each panel shows the result with the assumption of maximum rupture velocity at (a) 3 km/s, (b) 4 km/s, (c) 5 km/s, and (d) 6 km/s. The gray dashed lines show the reference rupture-front speeds.

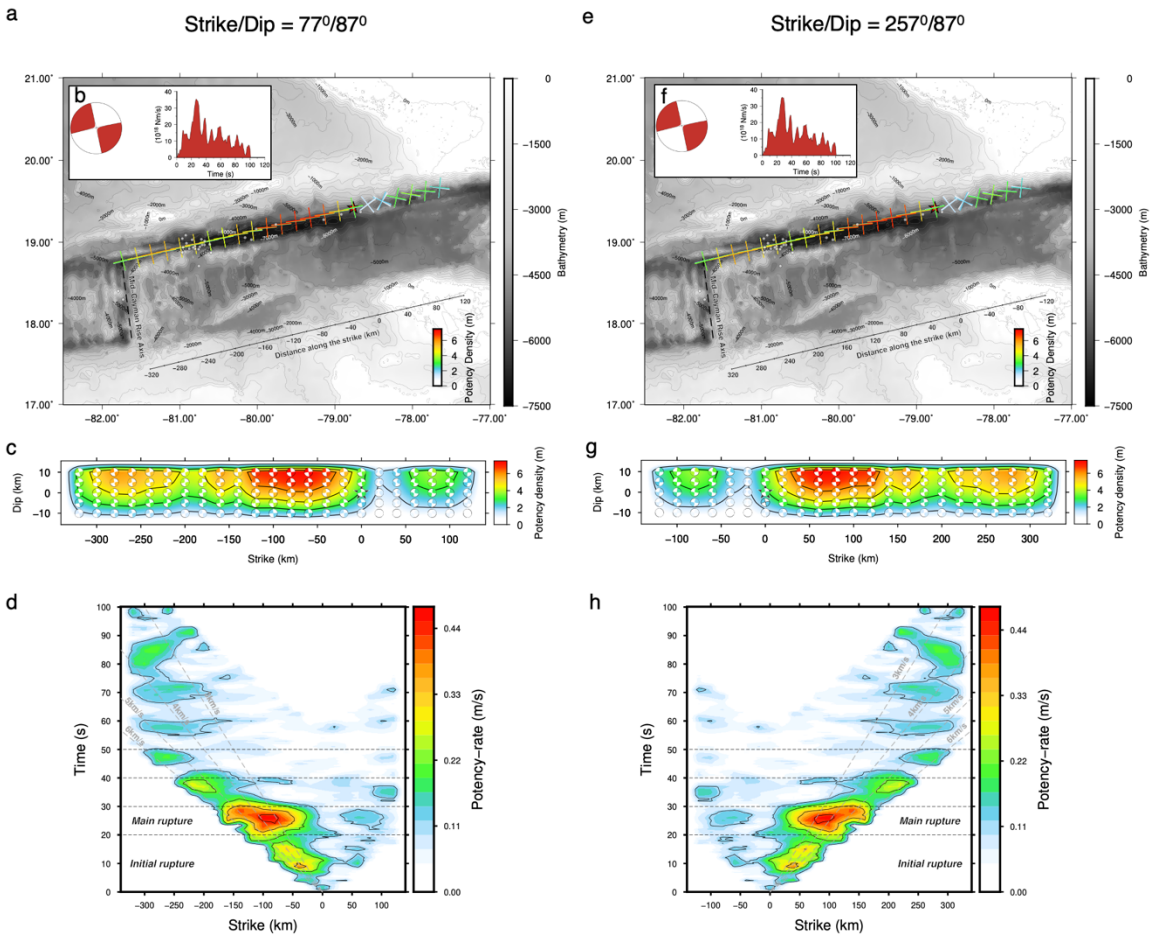

Figure S3. The results for the different model faults. (**a**) Map-view of the static potency density distribution of the model fault plane strike/dip : 77°/87°. The nodal plane (cross-mark) is extracted from the potency density tensor of each source knot by summing all the potency-density tensors along the dip direction for each strike direction. The contour line with 500 m intervals show the bathymetric feature (same as Fig. 2a). The gray circles are 1-week aftershocks, and the red star is the epicenter. (**b**) The information of moment-rate function and the total moment tensor solution of assumed model fault plane strike/dip : 77°/87°. (**c**) The cross-section (on model fault plane) of potency density and its focal mechanism of each source knot. The black star denotes the hypocenter. (**d**) The potency-rate density of rupture propagation along the strike. The gray dashed lines represent rupture speed. (**e**) to (**h**) The static distribution of potency density and its potency-rate density of rupture propagation of assumed model fault plane strike/dip : 257°/87° by the same details as (**a**) to (**d**).

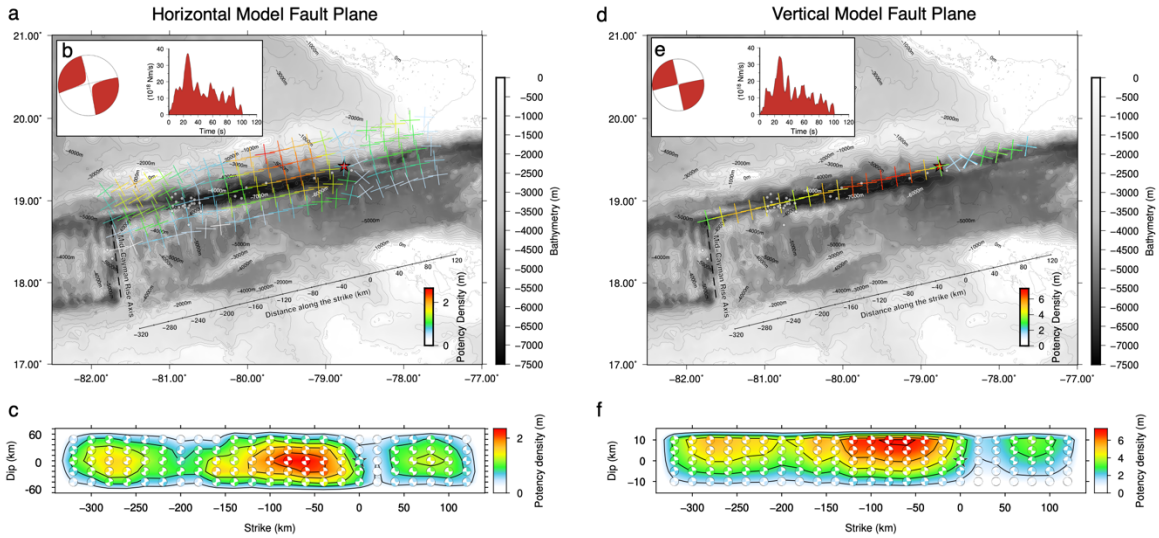

Figure S4. Comparison of the models with the horizontal and the vertical model fault planes. (a) The map view of static potency density distribution using the horizontal model fault (dip = 0°). The nodal planes (cross marker) for each location represent a potency density tensor, calculated by summing all the potency density tensors along the dip direction for each strike direction. All the potency density tensors are shown in Fig. 2d. The gray circle shows the 1-week aftershocks (USGS). The contour represents the bathymetry (GEBCO, 2020). (b) The total moment tensor solution estimated from our finite-fault model, using a lower-hemisphere stereographic projection, and the moment-rate function. (c) The cross-section of the static potency density distribution. The focal mechanism is presented by the beach ball at each source knot, plotted using a lower-hemisphere stereographic projection (not a view form side but from above). (d–f) Same as Fig. S4a–c, but for the result with using the vertical model fault (dip = 90°).

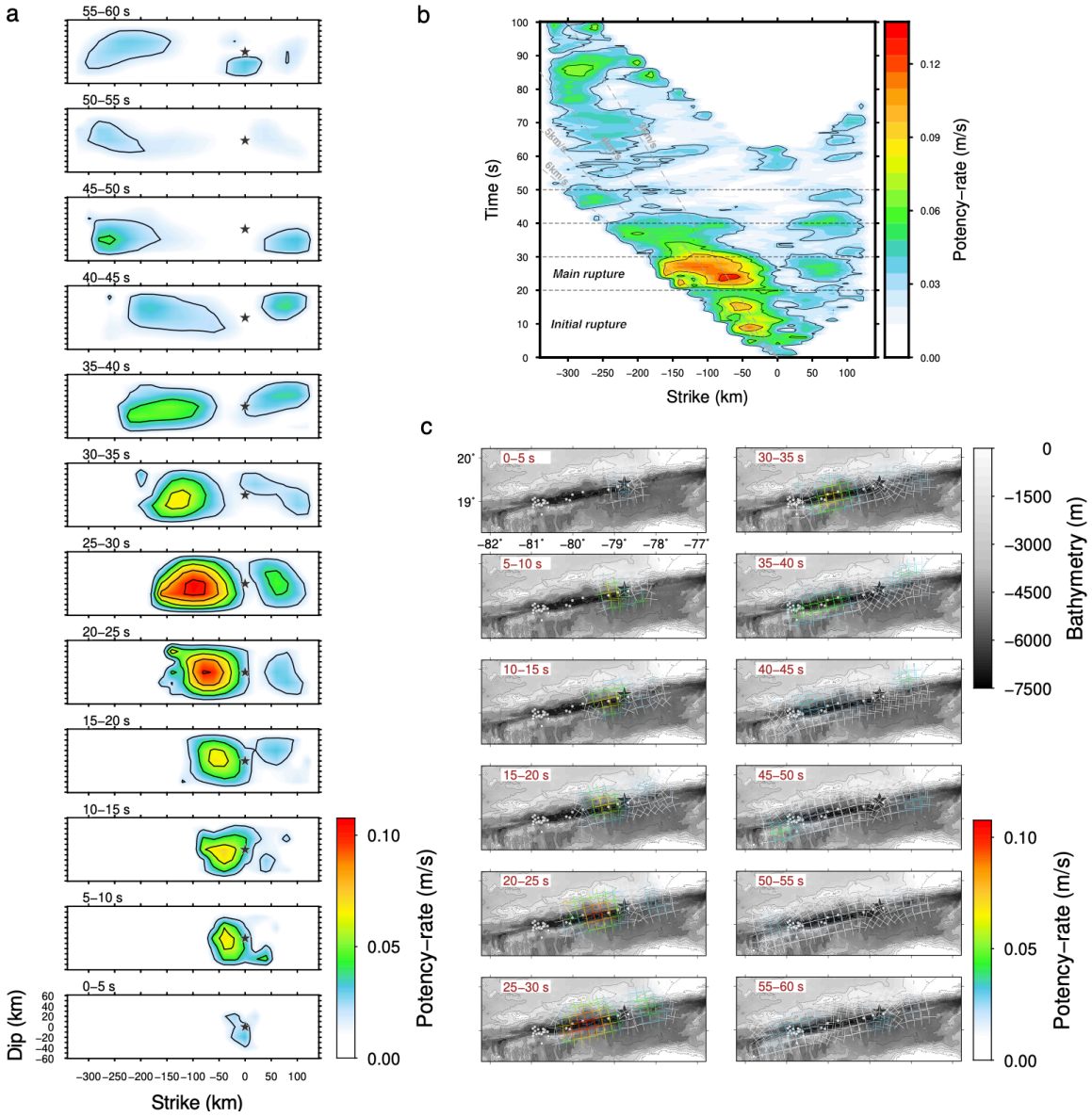

Figure S5. Spatiotemporal distribution of potency-rate density using the horizontal model plane. (a) The snapshots of the rupture propagation. The potency-rate density is averaged within each time window. The black star is the hypocenter, and the color contour shows the potency-rate density. (b) The potency-rate density distribution projected along the model strike. The gray dashed lines represent the reference rupture speeds. (c) The map-view snapshots of the averaged potency-rate density within each time window. The cross marker shows the focal mechanism extracted from the resultant potency-rate density tensor. The background contour shows the bathymetry (GEBCO, 2020). The black star and gray circle denote the epicenter and the 1-week aftershocks (USGS).

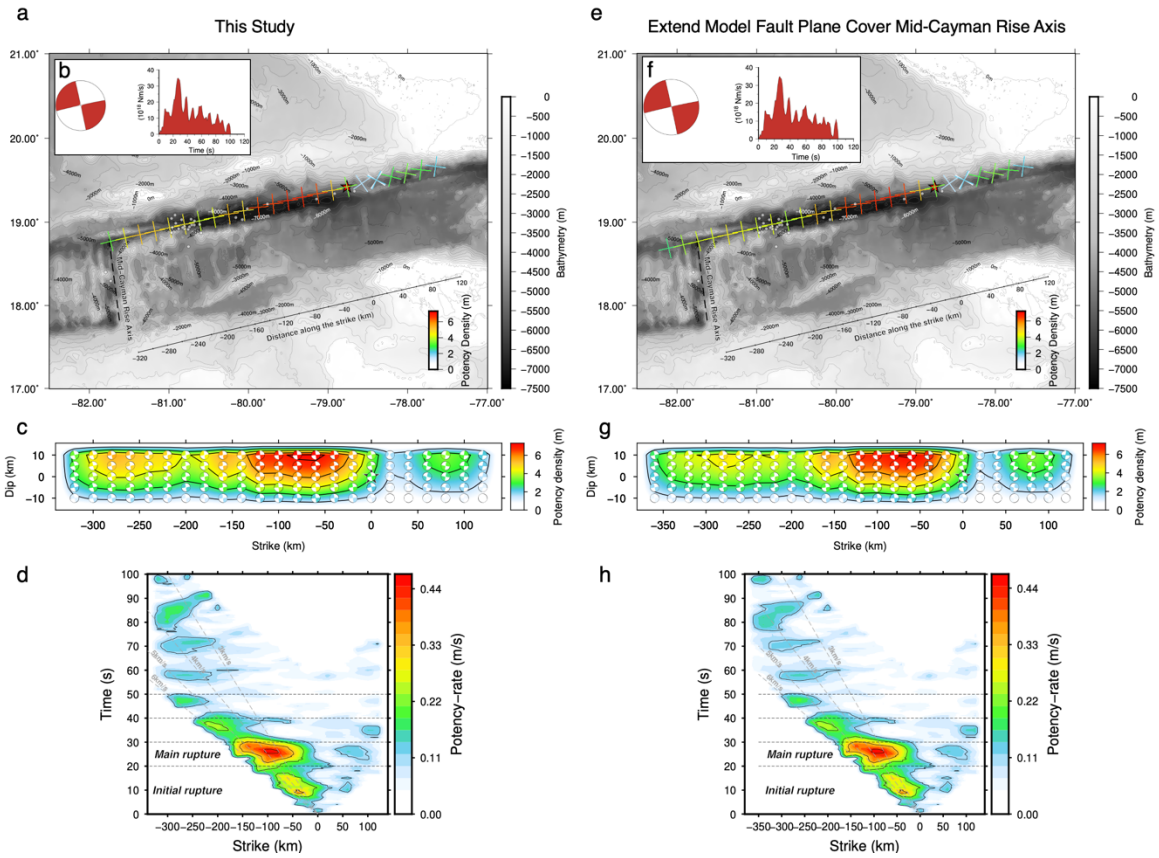

Figure S6. Comparison of the models with different model-fault lengths. (a) The map view of static potency density distribution. The nodal planes (cross marker) for each location represent a potency density tensor, calculated by summing all the potency density tensors along the dip direction for each strike direction. All the potency density tensors are shown in Fig. 2d. The gray circle shows the 1-week aftershocks (USGS). The contour represents the bathymetry (GEBCO, 2020). (b) The total moment tensor solution estimated from our finite-fault model, using a lower-hemisphere stereographic projection, and the moment-rate function. (c) The cross-section of the static potency density distribution. The focal mechanism is presented by the beach ball at each source knot, plotted using a lower-hemisphere stereographic projection (not a view form side but from above). (d) The potency-rate density distribution projected along the model strike. The gray dashed lines represent the reference rupture speeds. (e–h) Same as Fig. S6a–d, but for the result using the extended model-fault length.

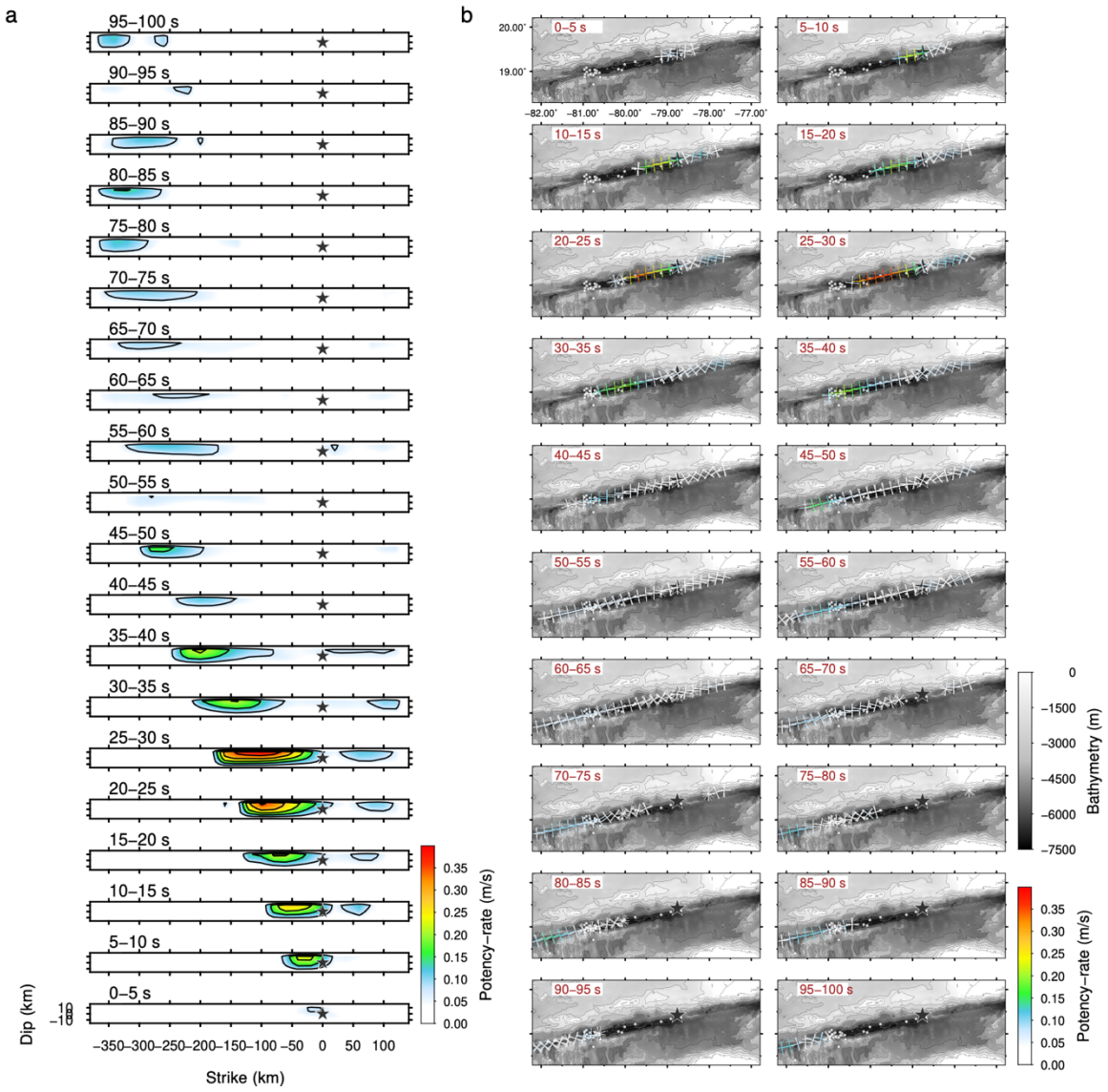

Figure S7. Spatiotemporal distribution of potency-rate density for the extended model-plane length (Fig. S7). (a) The snapshots of the rupture propagation. The potency-rate density is averaged within each time window. The black star is the hypocenter, and the color contour shows the potency-rate density. (b) The map-view snapshots of the averaged potency-rate density within each time window. The cross marker shows the focal mechanism extracted from the resultant potency-rate density tensor. The background contour shows the bathymetry (GEBCO, 2020). The black star and gray circle denote the epicenter and the 1-week aftershocks (USGS).

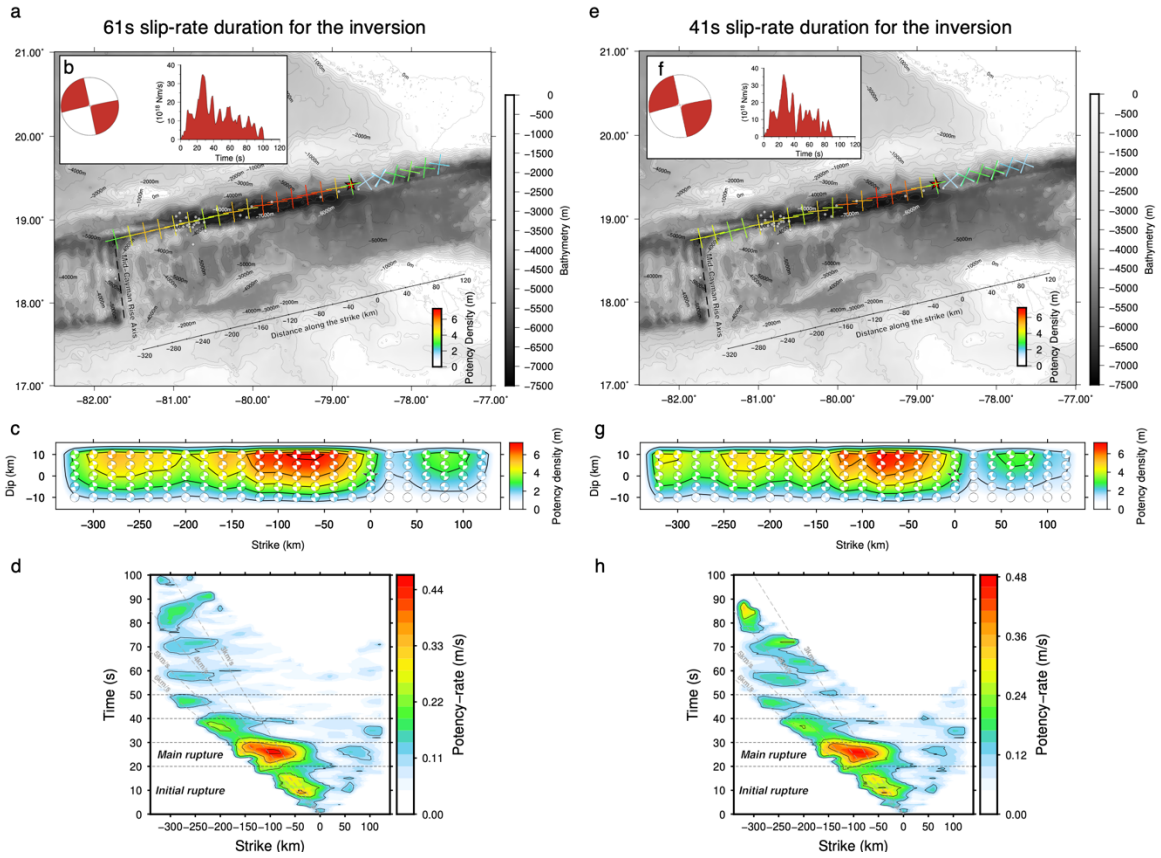

Figure S8. Comparison of the models with different assumption of duration of slip-rate function. (a) The map view of static potency density distribution by adopting the duration of slip-rate function at 61 s. The nodal planes (cross marker) for each location represent a potency density tensor, calculated by summing all the potency density tensors along the dip direction for each strike direction. All the potency density tensors are shown in Fig. 2d. The gray circle shows the 1-week aftershocks (USGS). The contour represents the bathymetry (GEBCO, 2020). (b) The total moment tensor solution estimated from our finite-fault model, using a lower-hemisphere stereographic projection, and the moment-rate function. (c) The cross-section of the static potency density distribution. The focal mechanism is presented by the beach ball at each source knot, plotted using a lower-hemisphere stereographic projection (not a view form side but from above). (d) The potency-rate density distribution projected along the model strike. The gray dashed lines represent the reference rupture speeds. (e–h) Same as Fig. S8a–d, but for the result adopting the duration of slip-rate function at 41 s.

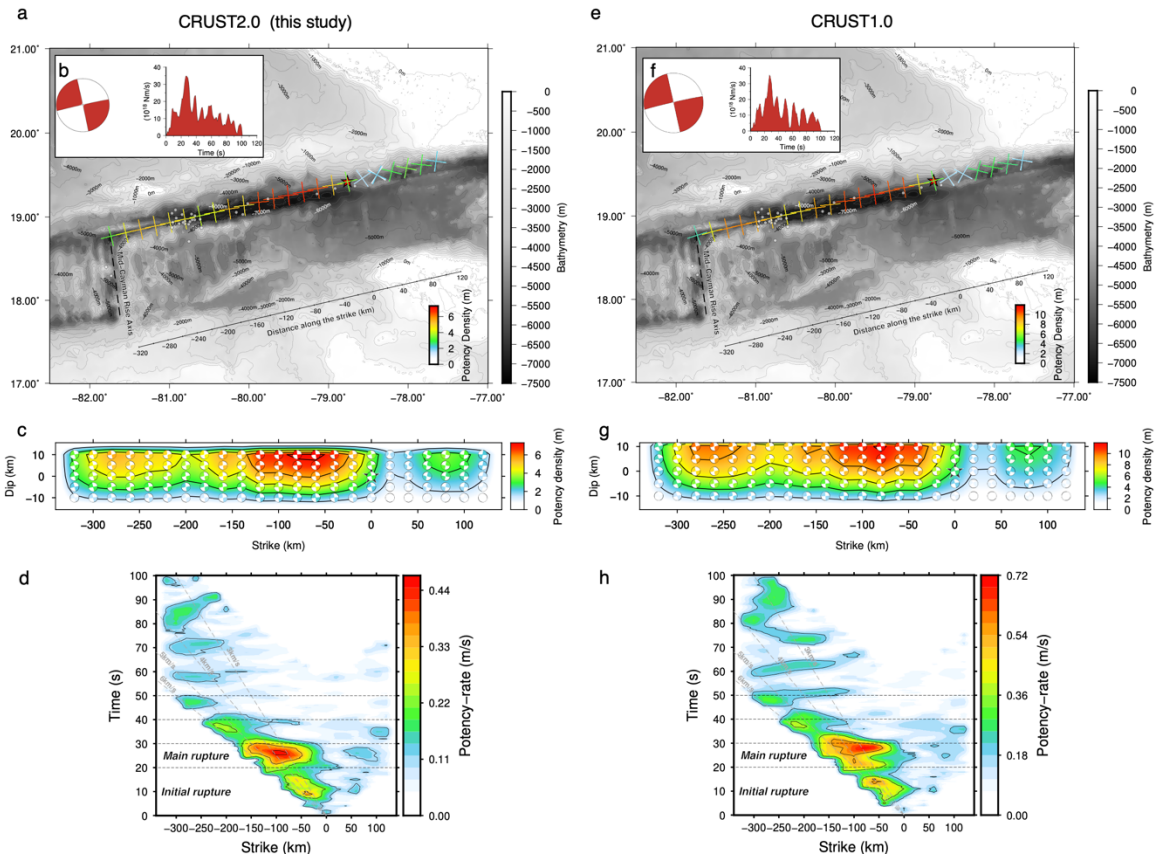

Figure S9. Comparison of the models with different near-field velocity structures. (a) The map view of static potency density distribution using the CRUST2.0 (Bassin et. al., 2000; USGS, 2020). The nodal planes (cross marker) for each location represent a potency density tensor, calculated by summing all the potency density tensors along the dip direction for each strike direction. All the potency density tensors are shown in Fig. 2d. The gray circle shows the 1-week aftershocks (USGS). The contour represents the bathymetry (GEBCO, 2020). (b) The total moment tensor solution estimated from our finite-fault model, using a lower-hemisphere stereographic projection, and the moment-rate function. (c) The cross-section of the static potency density distribution. The focal mechanism is presented by the beach ball at each source knot, plotted using a lower-hemisphere stereographic projection (not a view form side but from above). (d) The potency-rate density distribution projected along the model strike. The gray dashed lines represent the reference rupture speeds. (e–h) Same as Fig. S9a–d, but for the result using the CRUST1.0 (Laske et. al., 2013).

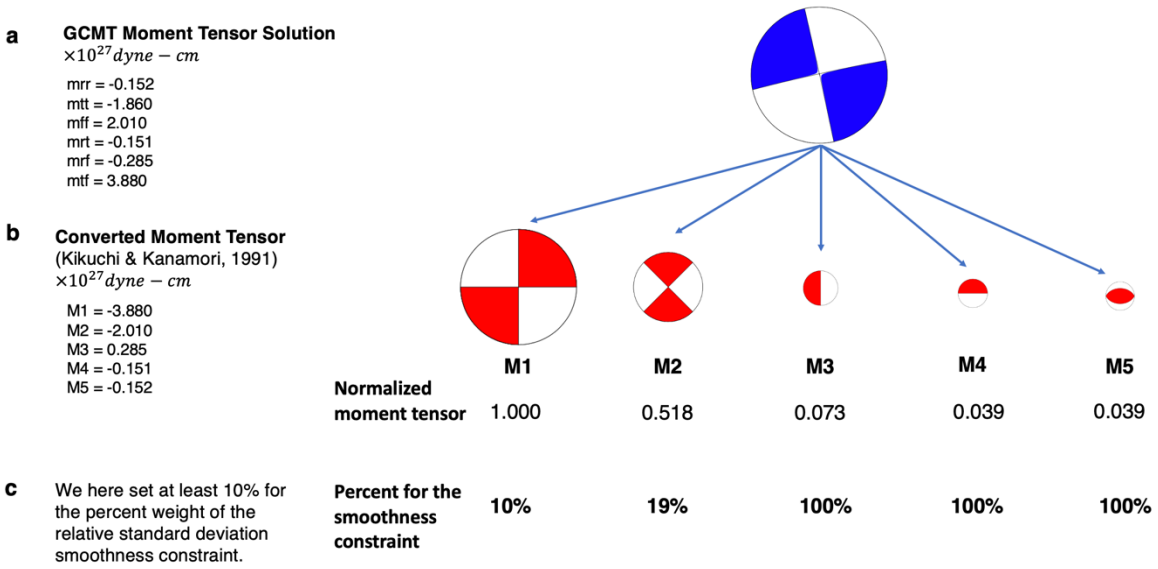

Figure S10. Summary of our new framework of inversion adopting relative weight for the smoothness constraint. The GCMT moment tensor solution of the 2020 Caribbean earthquake (GCMT, 2020) is divided into the 5 basis-moment tensors (M1 to M5, Kikuchi and Kanamori, 1991). Then, we determine the relative weight for each moment tensor component for the smoothness constraint.

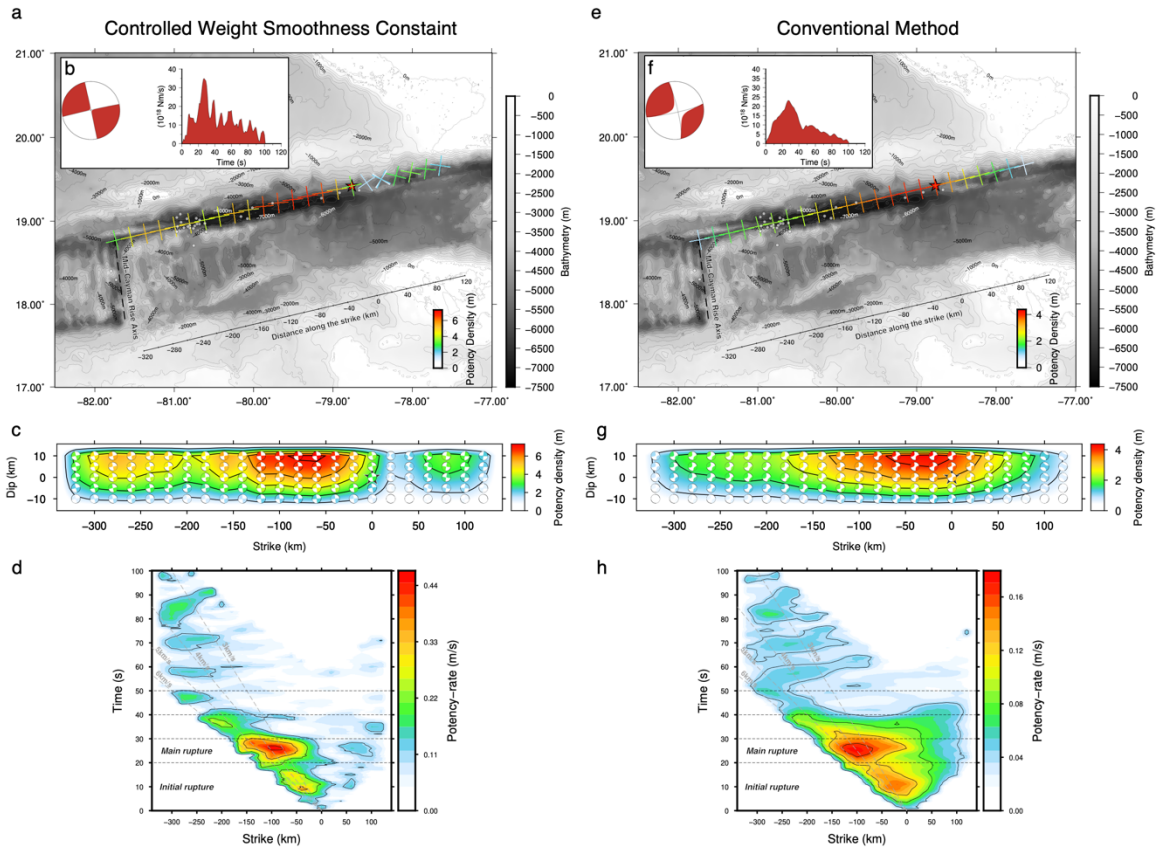

Figure S11. Comparison of the models adopting and not-adopting the relative weights for basis-moment tensors. (a) The map view of static potency density distribution by adopting the relative weights for basis-moment tensors. The nodal planes (cross marker) for each location represent a potency density tensor, calculated by summing all the potency density tensors along the dip direction for each strike direction. All the potency density tensors are shown in Fig. 2d. The gray circle shows the 1-week aftershocks (USGS). The contour represents the bathymetry (GEBCO, 2020). (b) The total moment tensor solution estimated from our finite-fault model, using a lower-hemisphere stereographic projection, and the moment-rate function. (c) The cross-section of the static potency density distribution. The focal mechanism is presented by the beach ball at each source knot, plotted using a lower-hemisphere stereographic projection (not a view form side but from above). (d) The potency-rate density distribution projected along the model strike. The gray dashed lines represent the reference rupture speeds. (e–h) Same as Fig. S11a–d, but for the result without adopting the relative weights for basis-moment tensors.

Table S1. CRUST2.0 structural velocity model being used in this study (Bassin et. al., 2000; USGS, 2020).

V_P (km/s)	V_S (km/s)	Density (10^3 kg/m^3)	Thickness (km)
1.50	0.01	1.02	4.0
2.20	1.10	2.20	1.0
5.00	2.50	2.60	2.5
6.60	3.65	2.90	4.0
7.10	3.90	3.05	5.0
8.08	4.47	3.38	0.0

Table S2. CRUST1.0 structural velocity model (Laske et. al., 2013).

V_P (km/s)	V_S (km/s)	Density (10^3 kg/m^3)	Thickness (km)
1.50	0.01	1.02	3.95
2.00	0.55	1.93	4.75
5.00	2.70	2.55	5.38
6.50	3.70	2.85	6.66
7.10	4.05	3.05	11.12
8.09	4.49	3.33	0.00

References

Bassin, C., Laske, G. and Masters, G. (2000), The Current Limits of Resolution for Surface Wave Tomography in North America, EOS Trans AGU, 81, F897.

GCMT. (2020), Mw 7.7 Cuba Region. Retrieved January 28, 2020, from https://www.globalcmt.org/cgi-bin/globalcmt-cgi-bin/CMT5/form?itype=ymd&yr=2020&mo=1&day=28&oyr=1976&omo=1&oday=1&jyr=1976&jday=1&ojyr=1976&ojday=1&otype=nd&nday=1&lmw=7&umw=10&lms=0&ums=10&lmb=0&umb=10&llat=-90&ulat=90&llon=-180&ulon=180&lhd=0&uhd=1000&l.

GEBCO Compilation Group, (2020), GEBCO 2020 Grid (Gridded Bathymetry Data Download). doi:10.5285/a29c5465-b138-234d-e053-6c86abc040b9.

Kikuchi, M., & Kanamori, H. (1991), Inversion of Complex Body Waves-III. *Bulletin of the Seismological Society of America*, *81*(6), 2335–2350. https://doi.org/10.1016/0031-9201(86)90048-8.

Laske, G., Masters., G., Ma, Z. and Pasyanos, M. (2013), Update on CRUST1.0 -A 1-degree Global Model of Earth's Crust, Geophys. Res. Abstract, 15, Abstract EGU2013-2658.

USGS. (2020), M 7.7 - 123km NNW of Lucea, Jamaica. Retrieved January 28, 2020, from https://earthquake.usgs.gov/earthquakes/eventpage/us60007idc/executive.